Journal of Materials Chemistry C

Defect healing and improved hole transport in CuSCN by copper(I) halide

Journal:	*Journal of Materials Chemistry C*
Manuscript ID	TC-ART-02-2025-000574.R1
Article Type:	Paper
Date Submitted by the Author:	05-Mar-2025

Complete List of Authors:	Sukpoonprom, Patipan; Vidyasirimedhi Institute of Science and Technology Kidkhunthod, Pinit; Synchrotron Light Research Institute, Chattakoonpaisan, Chitsanucha; Vidyasirimedhi Institute of Science and Technology Ittisanronnachai, Somlak ; Vidyasirimedhi Institute of Science and Technology, Frontier Research Center Sudyoadsuk, Taweesak; Vidyasirimedhi Institute of Science and Technology Promarak, Vinich; Vidyasirimedhi Institute of Science and Technology, Molecular Science and Engineering Pattanasattayavong, Pichaya; Vidyasirimedhi Institute of Science and Technology

Defect healing and improved hole transport in CuSCN by copper(I) halide

*Patipan Sukpoonprom,[a] Pinit Kidkhunthod,[b] Chitsanucha Chattakoonpaisan,[a] Somlak Ittisanronnachai,[a] Taweesak Sudyoadsuk,[a] Vinich Promarak,[a] and Pichaya Pattanasattayavong[a,]**

[a] Department of Materials Science and Engineering, School of Molecular Science and Engineering, Vidyasirimedhi Institute of Science and Technology (VISTEC), Rayong 21210, Thailand

[b] Synchrotron Light Research Institute (Public Organization), 111 University Avenue, Muang, Nakhon Ratchasima 30000, Thailand

* Corresponding author. E-mail: pichaya.p@vistec.ac.th

Keywords: Copper(I) thiocyanate, copper(I) halide, doping, defect healing, thin-film transistors

Abstract

Copper(I) thiocyanate (CuSCN) is a unique wide band gap, p-type inorganic semiconductor with extensive opto/electronic applications. Being a coordination polymer, CuSCN requires processing by coordinating solvents, such as diethyl sulfide (DES). The strong interactions between CuSCN and DES lead to the formation of SCN^- vacancies (V_{SCN}), which are detrimental to hole transport. In this work, we rationally modify copper(I) thiocyanate (CuSCN) through the use of chemically compatible copper(I) halides (CuX, where X = Cl, Br, or I). Assessing the device characteristics of thin-film transistors employing CuX-modified CuSCN as the p-channel layer, adding 5% of CuBr is found to be the most optimal condition. The hole mobility is increased by 5-fold to 0.05 $cm^2\ V^{-1}\ s^{-1}$ while the on/off current ratio is also enhanced up to 4×10^4. As the drain current in the off-state does not increase whereas the trap states density is reduced, the performance improvement can be attributed to the defect healing effect. Detailed characterizations by synchrotron-based X-ray absorption spectroscopy reveal the recovery of the coordination environment around Cu, confirming that Cl^- and Br^- can effectively passivate V_{SCN} defects. In particular, CuBr further improves film uniformity and smoothness. The simple protocol based on common chemicals reported herein is applicable to the standard CuSCN processing recipe, which is currently applied across a wide range of electronic and optoelectronic devices.

1. Introduction

Semiconductors based on coordination polymers (CPs) are an emerging class of materials with several attractive features, such as tunable optical and electronic properties, thermal and chemical stability, and solution-based processability.[1–5] One of the prime examples is copper (I) thiocyanate (CuSCN) which has been applied across a wide range of electronic and optoelectronic device applications.[6–9] CuSCN has a wide optical band gap (>3.5 eV) and moderately high field-effect hole mobility (in the saturation regime, μ_{sat}) of >0.01 $cm^2 V^{-1} s^{-1}$.[7,10,11] CuSCN can be deposited from solution at low temperatures, a trait that enables versatile processability and material modifications through simple methods. Importantly, CuSCN is among a few wide band gap, p-type inorganic semiconductors with well-demonstrated applications in thin-film transistors (TFTs). Nevertheless, its carrier transport characteristics need further improvements to get closer to the performance level of the n-type counterparts, particularly metal oxides.[12–14]

With its high potential, several studies have reported the doping of CuSCN to improve the device metrics further. Notably, Wijeyasinghe *et al.*[15] demonstrated strong p-doping of CuSCN by using a fluorinated fullerene derivative $C_{60}F_{48}$ which increased μ_{sat} by 10-fold up to 0.1 $cm^2 V^{-1} s^{-1}$ in TFTs. The improved hole-transport properties of CuSCN in that case were attributed to the trap-filling effect by excess holes; the highly fluorinated molecular dopant has very deep energy levels, being able to accept electrons from the valence band (VB) of CuSCN and generate a high hole concentration. However, the method leaves behind the trap states as well as possibly introduces more scattering centers (due to the dopants themselves) as evident from the larger subthreshold swing (S_{th}). The defect states in CuSCN likely arise from the native defects, such as Cu vacancies (V_{Cu}) and SCN vacancies (V_{SCN}).[16,17] Indeed, we recently identified V_{SCN} as important hole-trapping states in CuSCN and introduced solution-based I_2 doping as a defect healing method.[18] The optimal level of I_2 dopant results in I^- replacing the

vacant SCN^- sites, hence recovering the incomplete and distorted coordination around Cu^+. With such a defect passivation method, the performance of TFT devices remarkably showed an 8-fold enhancement of μ_{sat} and simultaneously a reduced trap state concentration. The work showed that addressing hole-trapping states is a promising strategy to advance hole-transport properties of CuSCN.

Further, Liang *et al*.[19] showed that Cl_2 can also result in a strong p-doping effect. The significant enhancement of conductivity through an increased hole-concentration led to a rise in the power conversion efficiencies (PCE) by approximately 20% and 40% in organic and perovskite solar cells, respectively, when compared to the undoped CuSCN employed as the hole transport layer (HTL). However, the potent p-doping was detrimental to TFT devices, as the CuSCN semiconducting channel became persistently conductive, hence negating the field effect. More recently, we investigated the effects of metal chlorides, namely, copper(I) chloride (CuCl), copper(II) chloride ($CuCl_2$), tin(II) chloride ($SnCl_2$), and tin(IV) chloride ($SnCl_4$), as dopants in CuSCN.[20] The simple solution-based doping method allows the incorporation of Cl^- ions into the CuSCN host while avoiding the usage of hazardous, highly toxic Cl_2 gas which requires specialized equipment or a closed environment setup, such as a dry-etching system.[19] The resulting $CuCl_2$- or $SnCl_4$-doped TFTs achieved μ_{sat} of up to 0.05 $cm^2\ V^{-1}\ s^{-1}$; however, a noticeable p-doping behavior was still observed as the field-effect modulation was hindered,[19] evident from the high drain current in the off-state ($I_{D,off}$) and reduced on-off current ratio (I_{on}/I_{off}). This was due to the metal ions in the high oxidation state that could accept electrons from the CuSCN host, causing excessive p-doping effect.

As demonstrated in the previous work, halide ions are promising for improving the hole transport properties of CuSCN, and it is essential to investigate the halide series systematically. In particular, the type of halide anions needs to be optimized for TFTs such that an increase in μ_{sat} is not traded off with a reduction in I_{on}/I_{off} or an increase in S_{th}. However, as Cl_2, Br_2, and

I_2 exist in the gas, liquid, and solid states, respectively; we instead employ solution-processable metal halide salts for inserting halide anions into CuSCN. As for the metal cation, Cu(I) is selected due to the chemical and structural compatibilities with CuSCN. Therefore, in this work we investigate the effects of doping CuSCN with copper(I) halides (CuX), with X = Cl, Br, and I (**Figure 1a**), on the physical properties and TFT device performance. Cu centers in CuSCN and CuX are all tetrahedrally coordinated, and the ionic radii of pseudohalide and halide anions are relatively suitable.[21] We found that all three dopants improved the hole transport properties with 5% CuBr-doped giving the best performance with μ_{sat} improved by five-fold to 0.05 cm^2 V^{-1} s^{-1}, accompanied by the lowest S_{th} and highest I_{on}/I_{off} ratio. Detailed characterizations showed that CuX doping can promote the crystalline orientation with in-plane Cu-S network which favors hole transport as well as restore the defective coordination environment around Cu via V_{SCN} defect healing with halide anions substitution.

2. TFT performance of CuX-doped CuSCN

TFTs were fabricated in the bottom-gate top-contact (BG-TC) architecture (**Figure 1b**) featuring Al (40 nm) as the bottom gate electrode and poly(vinylidene fluoride-trifluoroethylene-chlorofluoroethylene) [P(VDF-TrFE-CFE), 500 nm, geometric capacitance 96 nF cm^{-2}] as the gate dielectric. Pristine (undoped) and CuX-doped CuSCN layers (35±3 nm) were deposited as the p-channel, and Au (25 nm) were employed as the top source/drain electrodes. As the high-*k* polymer dielectric required a long period of annealing (3 h at 80 °C, see details in ESI),[7] the bottom-gate structure was employed to avoid the effects of the extended heating that might volatilize the halide species.[22,23] The top-contact was selected as it has been reported that staggered device architecture can minimize the contact resistance due to charge injection.[24] Devices were patterned with shadow masks to obtain channel lengths (L) between

30 to 100 μm and a channel width (W) of 1000 μm. The three dopants were tested at 1, 3, 5, and 7% doping [calculated from (mol_{CuX}/mol_{CuSCN})×100, see **Table S1** in the Electronic Supplementary Information (ESI) for detail]. The full results of representative transfer and output characteristics from all sample conditions are shown in **Figure S1-S4** (ESI). For transfer characteristics, small hysteresis can be observed, similar to previous reports on CuSCN TFTs.[6,18,25] Statistics of device parameters, including μ_{sat}, threshold voltage (V_{th}), S_{th}, and trap state density (D_{tr}) are shown in **Figure S5** and **Table S2** (ESI). Based on this data, the most optimal doping concentration that yielded the highest μ_{sat} for each dopant was 3% CuCl, 5% CuBr, and 1% CuI. These doping conditions are discussed in more detail below.

Figure 1c displays the transfer characteristics of TFTs from the best condition for each dopant. All devices exhibited well-behaved p-channel character. Our reference pristine CuSCN TFTs displayed standard characteristics similar to previous reports.[6,7,20,26] In CuX-doped devices, the drain current in the on-state ($I_{D,on}$) was increased by 2 to 5 times whereas $I_{D,off}$ was not significantly affected. The plots between $\sqrt{I_D}$ and gate voltage (V_G) (**Figure 1d**) show a positive shift in V_{th} (from the x-intercept) and an increase in μ_{sat} (from the slope). **Figures 1e-g** compare V_{th}, S_{th}, D_{tr}, μ_{sat}, and I_{on}/I_{off} of TFTs based on undoped CuSCN and the optimal condition of each dopant. D_{tr} was calculated from

$$D_{tr} = \frac{C_i}{q}\left(\frac{q}{k_B T}\frac{S_{th}}{\ln(10)} - 1\right) \quad (1)$$

where C_i is the geometric capacitance of the dielectric, q the elementary charge, k_B the Boltzmann constant, and T the temperature. Note that from Eq. (1), D_{tr} is obtained in the units of [cm^{-2} eV^{-1}] directly if C_i, q, k_B, T, and S_{th} are substituted in the units of [F cm^{-2}], [C], [J K^{-1}], [K], and [V dec^{-1}], respectively.

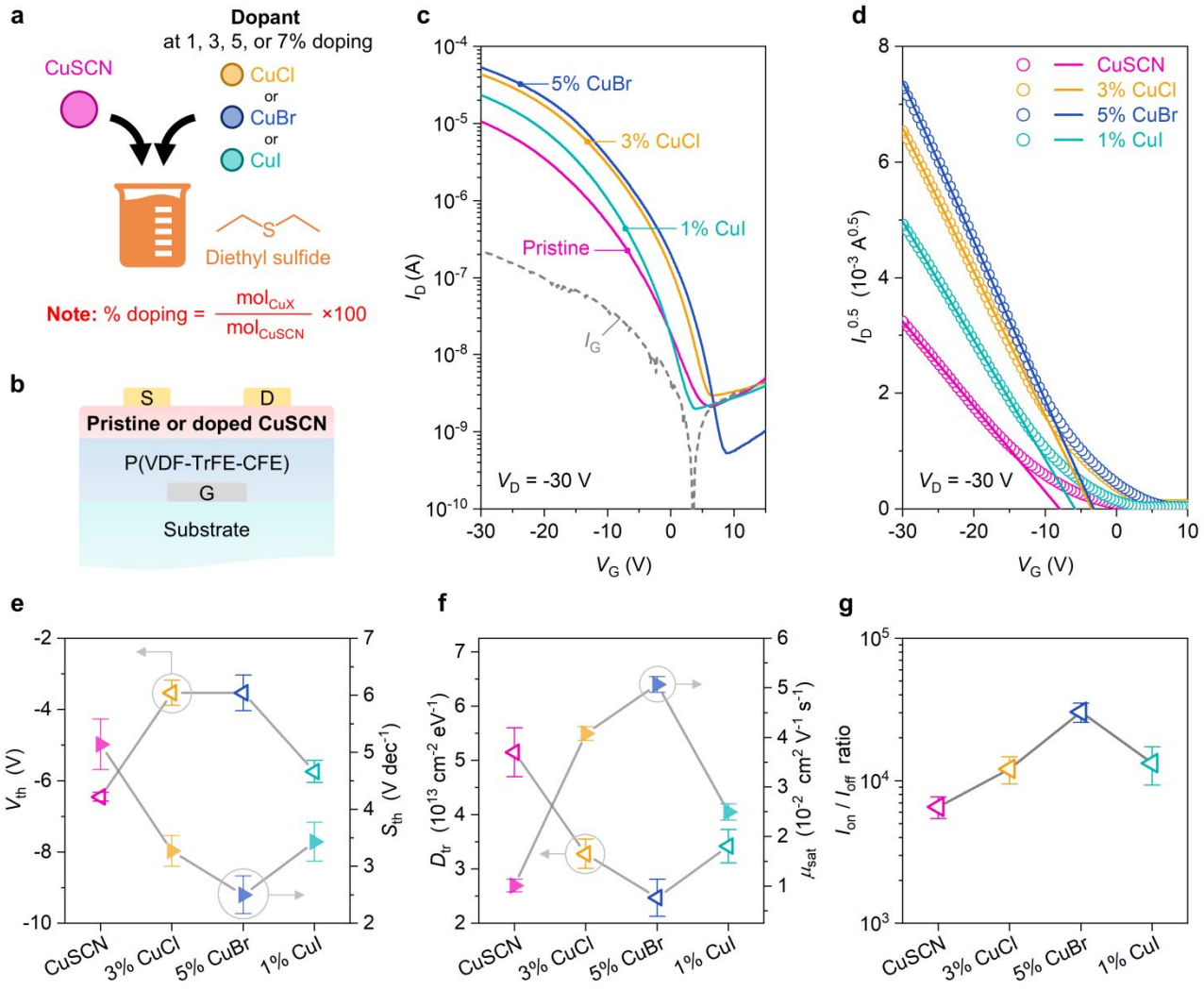

Figure 1. (a) Schematic of solution-based CuSCN doping process by CuX, where X = Cl, Br, or I. The solvent employed was diethyl sulfide (DES). The calculation for the % doping is also annotated. (b) Schematic structure of the bottom-gate top-contact (BG-TC) thin-film transistors (TFTs) employing CuSCN as the p-type channel. (c) Transfer characteristics (drain current I_D vs gate voltage V_G) at a drain voltage V_D = -30 V of TFTs based on pristine and doped CuSCN. Only forward sweeps are shown for clarity. (d) Plots of $\sqrt{I_D}$ vs V_G. (e-g) TFT device performance metrics: threshold voltage (V_{th}), subthreshold swing (S_{th}), trap states density (D_{tr}), saturation hole mobility (μ_{sat}), and on/off drain current ratio (I_{on}/I_{off}). For (c-g), Only the best condition (achieving highest μ_{sat}) for each dopant is shown: 3% for CuCl, 5% for CuBr, and 1% for CuI.

Notably, the observation that $I_{D,off}$ did not increase suggests that p-doping effect was not significant in this case.[15,27] In contrast, changes in other device parameters indicate that the addition of CuX led to V_{SCN} *defect healing*,[18,28,29] particularly evident from the concurrent positive shift in V_{th} and reduction in S_{th} (**Figure 1e**). Essentially, the shift in V_{th} (ΔV_{th}) could be correlated to the interfacial traps filling (ΔN_{tr}) (please see ESI for the calculation).[27,30] The values of ΔV_{th} and ΔN_{tr} for the optimized TFTs are shown in **Table S3** (ESI). The average ΔV_{th} of 3% CuCl and 5% CuBr were found to be similar at +2.92 V (requiring a smaller negative V_G to turn the p-channel device on), corresponding to a decrease in the trap density of 1.75×10^{12} cm^{-2} (V_{SCN} hole-trapping states filled by doping). For 1% CuI, ΔV_{th} and ΔN_{tr} were found to be +0.71 V and 4.3×10^{11} cm^{-2}, respectively. Similarly, the subthreshold swing S_{th} is related to the overall trap states density D_{tr};[31,32] both of which were reduced upon CuX doping (**Figure 1f**), reflecting the V_{SCN} defect passivation effect (see **Section 4** for discussion on V_{SCN} defects and their passivation by halide ions). Ultimately, hole transport in CuSCN was significantly enhanced as evident from the higher μ_{sat} (**Figure 1g**).

It is apparent that 5% CuBr yielded the best results overall, followed by 3% CuCl and 1% CuI. Comparing the average device parameters to those of pristine CuSCN, doping with 5% CuBr resulted in smaller V_{th} in terms of magnitude (from -6.45 to -3.53 V), reduced S_{th} (from 5.14 V to 2.50 V dec^{-1}) and correspondingly lower D_{tr} (from 5.15×10^{13} to 2.47×10^{13} cm^{-2} eV^{-1}), and enhanced μ_{sat} (from 0.01 to 0.05 cm^2 V^{-1} s^{-1}). Importantly, devices did not suffer from increased $I_{D,off}$ from the doping, and I_{on}/I_{off} was in fact increased from ~1×10^4 to ~3-4×10^4 due to the enhancement in $I_{D,on}$.

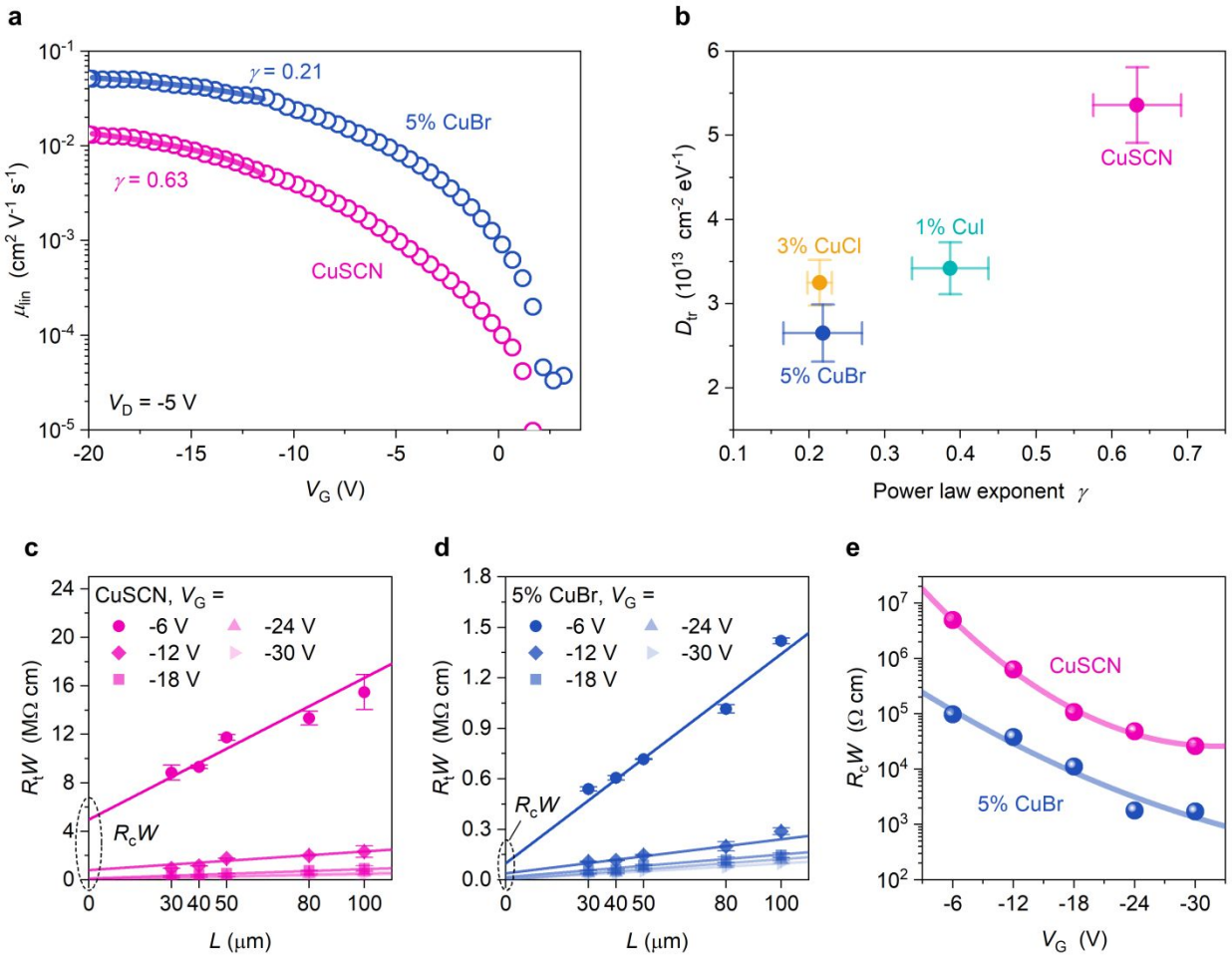

Figure 2. (a) Power law analysis of the relationship between linear mobility μ_{lin} and gate voltage V_G. (b) Trap states density D_{tr} vs power law exponent γ. (c) and (d) Gated transfer length method to find the contact resistance R_cW from the plots of the total resistance R_tW vs channel length L for pristine and 5% CuBr-doped CuSCN devices, respectively. Note that the resistances are normalized by the channel width W. (e) V_G dependence of R_cW from (c) and (d).

Next, the hole conduction mechanism was analyzed by fitting the V_G dependence of field-effect hole mobility in the linear regime (μ_{lin}) with the power law equation:[33]

$$\mu_{lin} = K(V_G - V_P)^{\gamma} \quad (2)$$

where V_P is the percolation threshold voltage, K is the proportional constant, and the exponent γ is associated with charge transport mechanism. Percolation conduction (PC) dominates when γ approaches 0.1 whereas trap-limited conduction (TLC) prevails when γ becomes close to 0.7.[33] In our case, the pristine CuSCN sample exhibited γ of 0.61, associated with the TLC-dominant charge transport mechanism, described by the thermal excitation from the localized tail states to the extended (mobile) states. In contrast, CuX-doped samples showed significantly smaller γ, for example, reduced to 0.21 for 5% CuBr doping (**Figure 2a-b**), indicating that the conduction mechanism transitioned to PC-dominant, which is more mobile as it occurs through the extended states impeded by some potential energy barriers from structural variations (in amorphous or polycrystalline structures).[34,35] The results corroborate that the hole transport was markedly improved through the reduction in trap states density as a result of V_{SCN} defect healing.

We also performed contact resistance (R_c) analysis to highlight the enhancement in device performance with CuX doping. The channel width-normalized R_cW was determined by the gated transfer length method (gTLM,[36] see detail in ESI) as shown in **Figure 2c-d** for pristine and 5% CuBr-doped CuSCN TFTs, respectively. As clearly evident, R_cW was substantially decreased by approximately 1 order magnitude to 1-2×10^3 Ω cm upon doping by 5% CuBr. We infer that the suppression of R_c was also attributable to the defect healing effect. The reduction in charge trapping states within the semiconducting channel and at the semiconductor/dielectric interface mitigates the gate-field screening effect, leading to more effective charge injection and the apparent decrease in R_c as observed.[37,38]

To summarize the effects of CuX doping on TFT device performance, our simple method resulted in a significant improvement in hole transport properties in CuSCN by reducing the hole trapping states. Importantly, TFT devices did not suffer from I_{on}/I_{off} reduction or subthreshold characteristics deterioration, typically associated with the p-doping

effect.[15,19,20] Instead, the performance enhancement can be attributed to V_{SCN} defect passivation by CuX. The substitution of suitable anions to the V_{SCN} sites (donor states, detrimental to hole transport)[17] within CuSCN has been shown to recover the coordination environment and subsequently suppress defect concentration.[18,26] Interestingly, CuCl and CuBr doping increased μ_{sat} by ~4-fold and ~5-fold, respectively, whereas CuI doping only improved μ_{sat} by ~2.5 times. In addition, device performance gradually dropped when the concentration of CuI was higher than 1% (also agreeing with our previous report which found an optimal doping concentration with I_2 to be 0.5 mol%).[18] One of the reasons could be due to the size of the anions: 181 pm for Cl^-, 196 pm for Br^-, and 220 pm for I^-, as compared to 213 pm for SCN^-.[39,40] The slightly smaller radii of Cl^- and Br^- could allow more favorable incorporation into CuSCN. However, the larger I^- led to more structural distortion and impurity phase formation, especially at high doping concentrations, as shown in the following sections.

3. Effects of CuX doping on optical, electronic, and structural properties of CuSCN

To understand the effects of CuX addition on the physical properties of CuSCN, samples of undoped CuSCN (as reference) and the optimal condition of each dopant: 3% CuCl, 5% CuBr, and 1% CuI, were further characterized. Ultraviolet-visible-near infrared (UV-vis-NIR) spectroscopy was employed to obtain the absorption spectra and determine the optical band gaps ($E_{g,opt}$) via Tauc plots (**Figure S6**, ESI). All doped samples displayed similar characteristics to those of reference CuSCN,[18,20,26,41] i.e., showing absorption peaks at 235 and 300 nm and having $E_{g,opt}$ in the range of 3.78-3.81 eV. Clearly, CuX doping did not affect the optical transparency or create new electronic states. Next, photoelectron yield spectroscopy (PYS) and Kelvin probe (KP) measurements were performed to elucidate the electronic energy levels. The ionization potential or the valence band maximum (VBM) obtained from PYS (**Figure S7a**, ESI) and the Fermi level (E_F) from KP allowed for the construction of a simplified

energy band diagram as shown in **Figure S7b** (ESI). Note that the conduction band minimum (CBM) was estimated from VBM + $E_{g,opt}$. In general, the band diagram remained largely unaffected. While doping shifted E_F slightly closer to VBM, the effect was not dramatic, agreeing with the previous section that the p-doping effect was not significant.

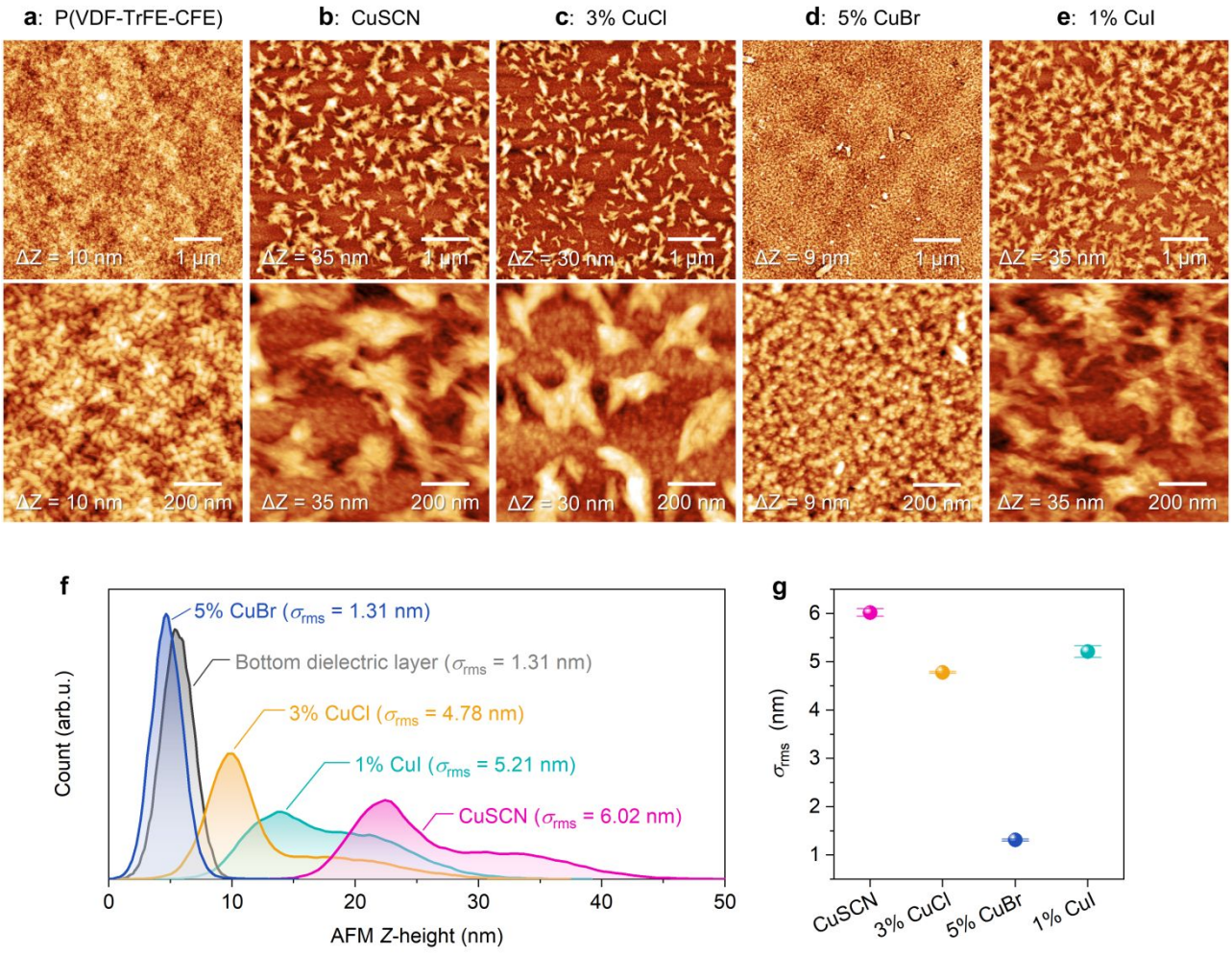

Figure 3. Surface heights from atomic force microscopy (AFM) of (a) P(VDF-TrFE-CFE) bottom dielectric layer, (b) CuSCN, (c) 3% CuCl, (d) 5% CuBr, and (e) 1% CuI. For (b) to (e), the films were deposited on top of the dielectric. Top row images: 5 μm × 5 μm. Bottom row images: 1 μm × 1 μm. (f) Surface height histograms and (g) root-mean-square roughness (σ_{rms}) of 5 μm × 5 μm images.

To study the morphology, CuSCN films engineered by CuX were investigated by atomic force microscopy (AFM). The films were deposited on the P(VDF-TrFE-CFE) dielectric layer in the same fashion as the TFT device structure. As shown in **Figure 3a-e**, the reference CuSCN, 3% CuCl, and 1% CuI films showed the familiar character of rice-grained features but with some clustering,[18,20] likely due to the interactions with the bottom dielectric layer.[25] However, the film doped with 5% CuBr exhibited noticeably different morphology: flat surface with small grains. **Figure 3e-f** display the histograms of the surface height distributions and root-mean-square roughness (σ_{rms}) obtained from the AFM images, respectively. While CuCl and CuI decreased σ_{rms} slightly, CuBr resulted in a dramatically smoother film with σ_{rms} reduced from 6.02 nm (reference CuSCN) to 1.31 nm (also similar to the value of the underlying dielectric layer). The improvement in film uniformity and ultrasmooth surface roughness should facilitate hole transport in CuBr-doped CuSCN when compared to other samples.[26,31,42]

X-ray diffraction (XRD) was then carried out to study the structural properties of CuX-doped CuSCN. In this case the samples were prepared by drop-casting to increase signal intensity. The pristine CuSCN prepared from DES-based solution expressed a distinct diffraction pattern identifiable as 3R β-CuSCN (ICSD 24372),[43] similar to our previous results.[18,20] As annotated in **Figure 4a**, the prominent peaks at 2θ = 16.3°, 27.3°, 32.7°, 34.7°, 47.2°, and 50.0° can be assigned to diffractions from (0 0 6), (1 0 $\bar{2}$), (0 0 12), (1 0 $\bar{8}$), (2 $\bar{1}$ 0), and (2 $\bar{1}$ 6) planes, respectively. While **Figure 4a** only shows the data of undoped CuSCN and the optimal condition of each dopant, the full results of all samples are included in **Figure S8a-c** (ESI). It is evident from the strong intensity of the (0 0 6) diffraction that the preferred orientation in all samples was with the *c*-axis of the CuSCN structure perpendicular to the plane of the substrate ('*vertical*' orientation, see **Figure S8d** ESI). Interestingly, this preferential orientation was further intensified upon CuX doping as the diffractions from other planes

diminished (**Figure 4b**); the XRD patterns became strongly dominated by diffractions from (0 0 6) and (0 0 12) planes with some detectible signal from (1 0 $\bar{2}$) planes. As diffraction from the latter signifies that the *c*-axis of β-CuSCN lies relatively flat with respect to the substrate (making a small angle to the substrate plane, '*horizontal*' orientation, see **Figure S8e** ESI), we then calculated the intensity ratios between (0 0 6) and (1 0 $\bar{2}$) diffractions as a proxy to compare the preferential orientation. As shown in **Figure 4c**, it becomes apparent that CuX doping preferentially led to the '*vertical*' orientation. Since the large dispersion in the valence band states (corresponding to low hole effective mass or high hole mobility) is strongly related to the plane of the Cu-S network in CuSCN,[2,44] this preferred orientation could also contribute to the increase in μ_{sat} observed in CuX-doped TFT devices.

When analyzing the (0 0 6) diffraction in more detail, we estimated the crystallite size using the Scherrer equation and found that the size slightly increased from 62 nm for undoped CuSCN to around 70 nm for the optimal doping conditions. We also noticed that the peaks of CuCl- and CuI-doped samples remained largely similar to that of reference CuSCN whereas those of CuBr-doped samples slightly shifted to lower diffraction angles (**Figure S8b**, ESI), signifying an expansion in the CuSCN lattice. The exact reason is still unknown. As the radius of Br^- is intermediate between that of Cl^- and I^-, the anion size may not be the only factor. We speculate that the specific interactions between the constituents (Cu^+-Br^- and SCN^--Br^-) could play a role. However, this effect on the lattice may be related to the change in the morphology observed from the AFM images. The stress from the lattice expansion could prevent the grain growth, resulting in small grains and smooth morphology in CuBr-doped CuSCN film.

We also remark that for CuI doping, concentrations higher than 1% resulted in two extra XRD peaks at 19.9° and 25.0°, which can be identified as a segregated CuI impurity phase. The latter was confirmed by measuring a drop-cast sample of CuI (also processed with DES) which produced a similar XRD pattern (**Figure S8c**). The presence of the impurity phase

could explain the limited TFT device performance in CuI-doped devices, especially with concentrations higher than 1%. While excess amount of dopants generally leads to reduced mobility due to impurity scattering,[45,46] the case of CuI doping was exacerbated by the additional formation of the heterogeneous CuI phase.

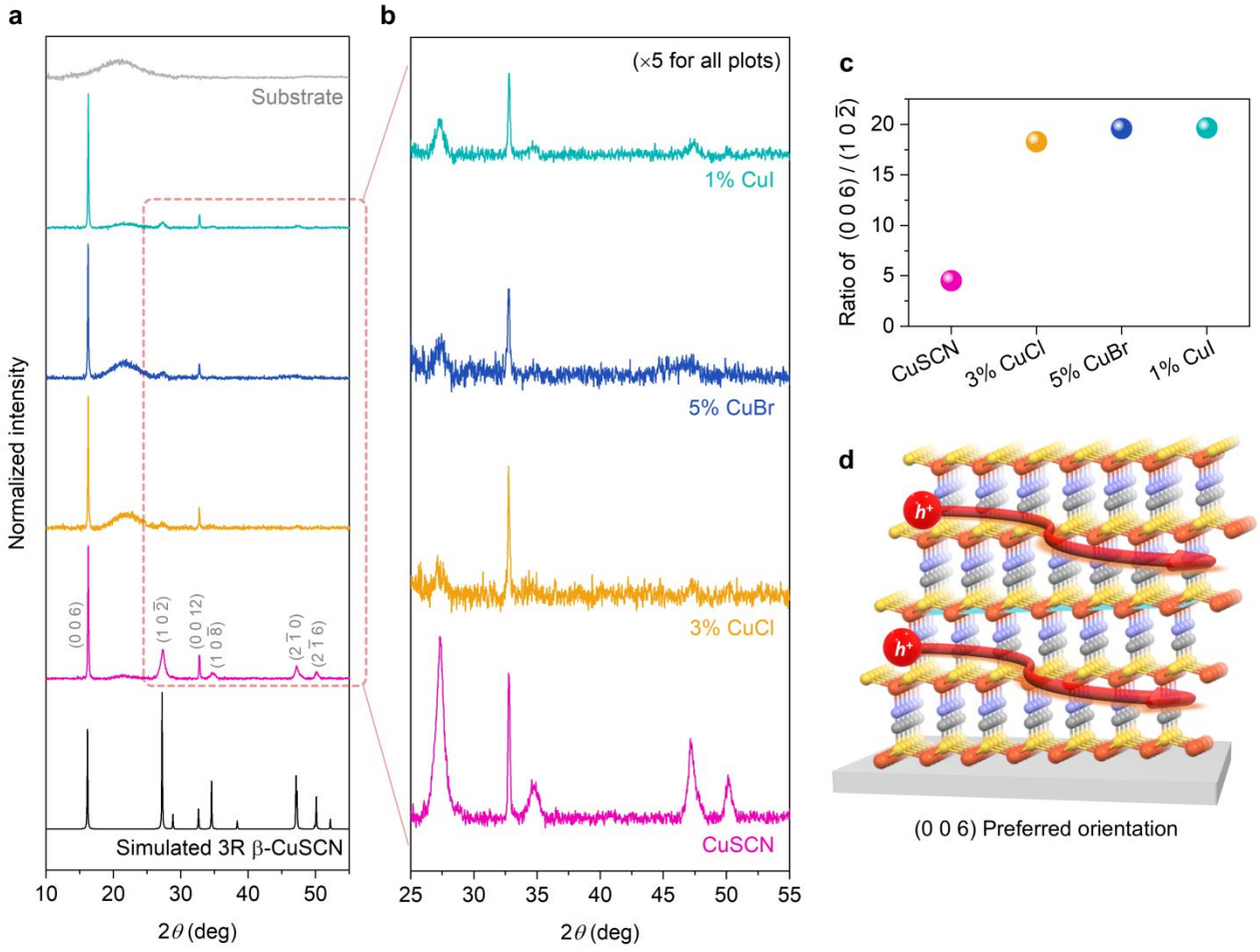

Figure 4. (a) X-ray diffraction (XRD) patterns of drop-cast samples. Simulated data of 3R β-CuSCN phase is shown for diffraction planes identification. The broad feature around 20° is from the glass substrate. (b) Close-up of XRD patterns in the 2θ range of 25° to 55°. (c) Ratio of peak intensity between (0 0 6) and (1 0 $\bar{2}$) diffractions. (d) Schematic of hole transport through the Cu-S network in CuSCN.

4. Chemical states and defect healing effect

Chemical states of the samples were probed by X-ray photoelectron spectroscopy (XPS). The XPS survey scans confirmed the presence of Cu, S, N, C, and the relevant halide dopant in all samples (**Figure S9-S11**, ESI). Very small signals of O were detected, likely due to contamination from the atmospheric oxygen during sample transport. The high-resolution core-level spectra of Cu 2p, S 2p, N 1s and C 1s found the expected chemical states at typical binding energies (BE) similar to previous reports of CuSCN.[26,47] In general, the Cu 2p core-level spectra showed that Cu was in the Cu(I) state with the intense Cu $2p_{3/2}$ peak found at BE of ~932.7-932.9 eV. The satellite feature of Cu(II) was not detected.[6,26] Moreover, Cu(I) species belonging to CuCl, CuBr, or CuI (with Cu $2p_{3/2}$ BE between 932.0-932.4 eV)[48–50] were not found. We inferred that Cu atoms from the dopants were located at the Cu(I) sites of CuSCN (further corroborated by X-absorption experiments discussed below). This confirmed the chemical compatibility of Cu(I) halides as dopants in the CuSCN host. However, to determine whether these additional Cu(I) species also fill V_{Cu} sites or displace the original Cu(I) atoms of the host, further investigation is still needed. A system with a high concentration of V_{Cu} (i.e., CuSCN having high initial conductivity or high $I_{D,off}$) should be synthesized first to allow for an objective analysis.[51]

Next, the high-resolution S 2p and N 1s core-level spectra indicated the S−C≡N bonding state, associated with S $2p_{3/2}$ around ~163.8 eV and N 1s ~398.6-398.9 eV. For the latter state, a small and broad feature at a higher BE was observed in some samples. This has been assigned to N-H in previous reports.[6,47] For C 1s, the spectra revealed two features: S−C≡N at 286.1-286.2 eV and adventitious carbon at 284.8 eV (used for referencing the XPS spectra). Overall, the chemical states of the CuSCN host remain largely unaffected by the addition of copper(I) halides at the concentrations studied in this work.

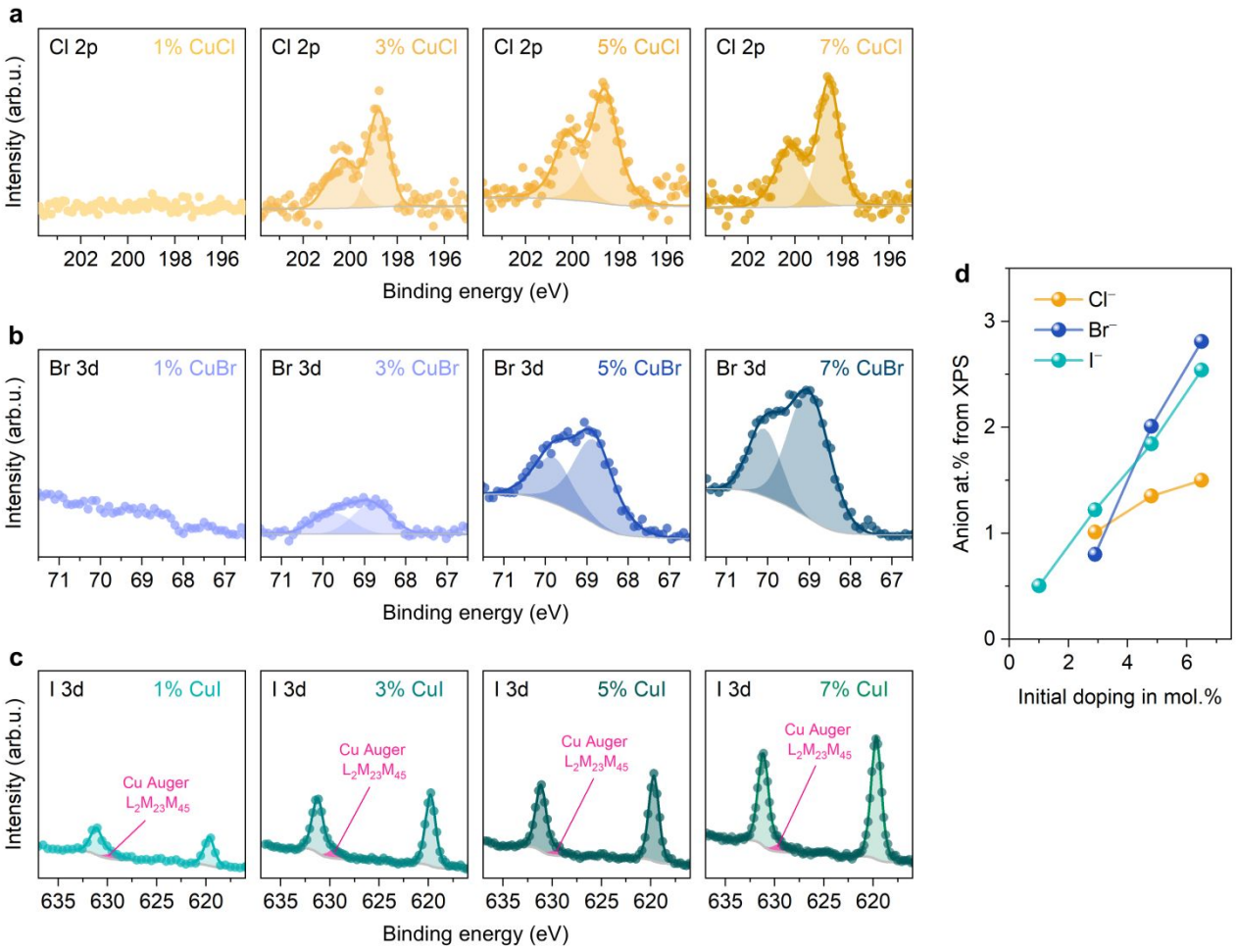

Figure 5. X-ray photoelectron spectroscopy (XPS) high-resolution core-level scans of (a) Cl 2p, (b) Br 3d, and (c) I 3d in doped CuSCN samples. Solid circles indicate the experimental data points, shaded areas the deconvoluted fitting components, colored lines the sum of the fitting, and grey lines the background. (d) Plots between amount of dopants initially added in mol.% vs amount found by XPS in at.%.

XPS results also confirmed the existence of each dopant, and the high-resolution core-level spectra are shown in **Figure 5a-c** for Cl 2p, Br 3d, and I 3d. At 1% doping, the signal intensity for Cl and Br was too low to be detected whereas the feature of I was easily detected due to its high sensitivity in XPS measurements.[52,53] We note that the I 3d spectra overlapped

with Cu $L_2M_{23}M_{45}$ (^{1}P) Auger electron peak at BE ~629 eV,[52,54] which we carefully accounted for in the quantitative analysis of iodine. In general, the signal intensity of halides gradually increased with the increasing amount of added dopant. **Figure 5d** shows the plots between the atomic percentage of the dopants found from XPS vs the nominal doping concentration (converted to mol.%) (see also **Table S1**, ESI). The quantities found from XPS were lower than the amounts initially added in the solution, possibly limited by the thermodynamic equilibrium of the modified structure. Also, some halides may have been lost during film annealing due to their volatile nature.[55,56]

Furthermore, the local environment around Cu atom was characterized in detail by synchrotron-based X-ray absorption spectroscopy (XAS, details in ESI) with the full results shown in **Figure S12** (ESI). **Figure 5a** displays the X-ray absorption near edge structure (XANES) data of undoped CuSCN and the optimally doped condition for each CuX dopant. The rising edge at 8984 eV could be attributed to the 1s→4p electronic transition of Cu^+. The 1s→3d transition of Cu^{2+} was not detected as no features of the pre-edge at energies below 8980 eV were observed, indicating the oxidation of Cu^+ to Cu^{2+} did not occur through doping process.[57,58] The overall XANES spectra were consistent with the pattern of 4-coordinate Cu^+ (d^{10}) previously reported in the literature.[18,20,26,59] The results corroborate our XPS discussion that Cu existed in the Cu(I) state in all samples. Comparing the white line (the highest absorption peak at 8997 eV), samples doped with 3% CuCl and 5% CuBr exhibited noticeably higher intensities than that of undoped CuSCN, signifying improvement in the coordination number of Cu.[60–62] A similar observation was previously reported and could be explained by the defect healing effect.[18]

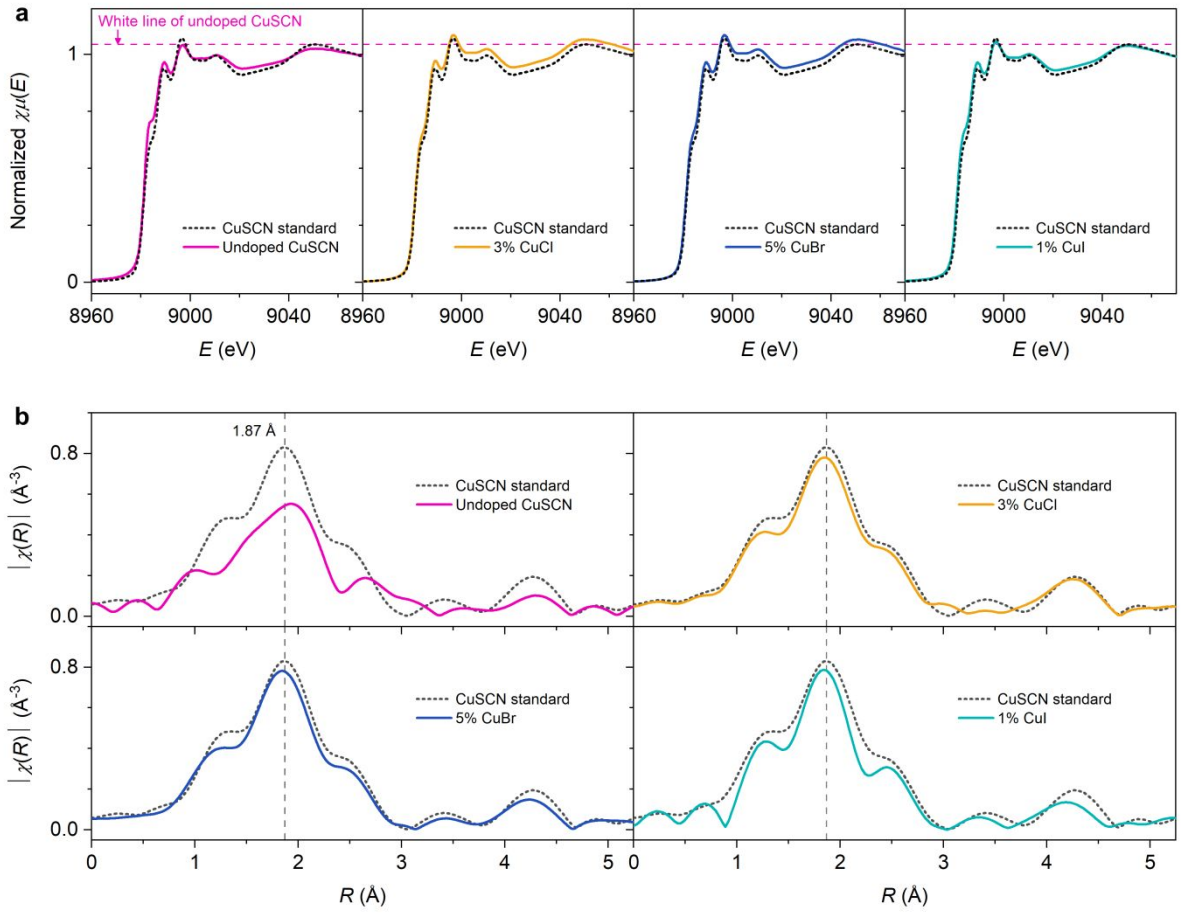

Figure 6. (a) X-ray absorption near-edge structures (XANES) and (b) extended X-ray absorption fine structures (EXAFS) in *R*-space at Cu K-edge of undoped CuSCN and the optimal concentration for each dopant. The radian distance (*R*) is shown without phase shift correction.

Defect passivation could be further confirmed by the extended X-ray absorption fine structure (EXAFS) results as shown in **Figure 5b** (data in *k*-space is shown in **Figure S12**, ESI). The spectrum of CuSCN standard typically exhibits a dominant peak at 1.87 Å and another feature around ~1.5 Å, attributed to the scattering paths of Cu−S and Cu−N bonding, respectively.[18,20,63] For the undoped CuSCN sample, we observed that overall environment of Cu atom became less well defined when compared to the standard. This evidence signifies

defective coordination environment around Cu in the reference sample prepared from dissolving CuSCN in DES. As reported in our previous work, DES can coordinate strongly to Cu(I),[26] and the subsequent removal during annealing can lead to the formation of incomplete bonding, i.e., V_{SCN} defects, around Cu.[18] As V_{SCN} are donor states, they are detrimental to the hole transport.[17,18,64] With the optimal addition of CuX dopants, especially CuCl and CuBr, the EXAFS spectra displayed similar profiles to that of the CuSCN standard, indicating the remarkable recovery of the local structure around Cu atoms. Specifically, the voids associated with V_{SCN} around Cu were effectively passivated. We previously reported a detailed study in which I^- could fill in the defective V_{SCN} site, restoring the Cu coordination environment.[18] Based on similar XAS results in this work, we infer that Cl^- and Br^- could also passivate V_{SCN} defects in CuSCN. As seen from the TFT results, the trap states density was reduced while hole mobility was significantly improved in CuCl- and CuBr-doped devices. We note that while CuI doping somewhat produced similar effects at 1% doping (as expected from I^-), the samples mainly suffered from the formation of the impurity CuI phase at higher concentrations which greatly hindered hole transport.

5. Conclusions

We have shown that CuX dopants, with X = Cl, Br, or I, could significantly improve the performance of CuSCN p-channel TFT devices. The optimal concentrations were found to be: 3% CuCl, 5% CuBr, and 1% CuI. Specifically for CuBr doping, μ_{sat} was increased by ~5 times up to 0.05 $cm^2\ V^{-1}\ s^{-1}$. Importantly, I_{on}/I_{off} ratio was also increased to $3\text{-}4\times10^4$ as $I_{D,off}$ did not increase upon the addition of CuX dopants, suggesting that there was minimal p-doping effect. The enhancement in device performance was accompanied by a reduction in D_{tr} by about 2 times, from 5.2×10^{13} down to 2.5×10^{13} $cm^{-2}\ eV^{-1}$. The latter could be explained by the defect

healing effect. XAS results clearly showed that the defective coordination environment around Cu due to V_{SCN} defects was effectively passivated by Cl^- and Br^-. While I^- could also heal the defects, CuI impurity phase easily formed, adversely affecting the hole transport. Our solution-based doping method reported herein employs common chemicals, CuCl and CuBr, which can be added directly to the standard CuSCN processing recipe. As CuSCN is now employed as a hole transport layer in a wide range of devices, the method can be easily applied to improve the performance or efficiency of various electronic and optoelectronic applications.

Author contributions

Patipan Sukpoonprom: methodology, investigation, validation, formal analysis, data curation, visualization, and writing – original draft. Pinit Kidkhunthod: methodology, investigation, validation, and data curation (XAS). Chitsanucha Chattakoonpaisan: investigation. Somlak Ittisanronnachai: methodology, investigation, and supervision. Taweesak Sudyoadsuk: methodology and supervision. Vinich Promarak: resources and funding acquisition. Pichaya Pattanasattayavong: conceptualization, funding acquisition, resources, project administration, supervision, visualization, and writing – review & editing.

Conflicts of interest

There are no conflicts to declare.

Data availability

The data supporting this article have been included as part of the Supplementary Information.

Acknowledgements

This research is funded by the National Research Council of Thailand (NRCT) under grant number N42A650255. This material is based upon work supported by the Air Force Office of Scientific Research under award number FA2386-22-1-4082. P.S. and P.P. acknowledge Vidyasirimedhi Institute of Science and Technology (VISTEC) for Ph.D. scholarship and research funding and VISTEC's Frontier Research Center (FRC) for scientific instruments.

References

(1) Wechwithayakhlung, C.; Packwood, D. M.; Chaopaknam, J.; Worakajit, P.; Ittisanronnachai, S.; Chanlek, N.; Promarak, V.; Kongpatpanich, K.; Harding, D. J.; Pattanasattayavong, P. Tin(II) Thiocyanate $Sn(SCN)_2$-a Wide Band Gap Coordination Polymer Semiconductor with a 2D Structure. *J. Mater. Chem. C* **2019**, *7* (12), 3452–3462. https://doi.org/10.1039/c8tc06150e.

(2) Pattanasattayavong, P.; Packwood, D. M.; Harding, D. J. Structural Versatility and Electronic Structures of Copper(I) Thiocyanate (CuSCN)-Ligand Complexes. *J. Mater. Chem. C* **2019**, *7* (41), 12907–12917. https://doi.org/10.1039/c9tc03198g.

(3) Huang, X.; Sheng, P.; Tu, Z.; Zhang, F.; Wang, J.; Geng, H.; Zou, Y.; Di, C.; Yi, Y.; Sun, Y.; Xu, W.; Zhu, D. A Two-Dimensional π–d Conjugated Coordination Polymer with Extremely High Electrical Conductivity and Ambipolar Transport Behaviour. *Nat. Commun.* **2015**, *6* (1), 7408. https://doi.org/10.1038/ncomms8408.

(4) Li, Y.; Jiang, X.; Fu, Z.; Huang, Q.; Wang, G.-E.; Deng, W.-H.; Wang, C.; Li, Z.; Yin, W.; Chen, B.; Xu, G. Coordination Assembly of 2D Ordered Organic Metal Chalcogenides with Widely Tunable Electronic Band Gaps. *Nat. Commun.* **2020**, *11*

(1), 261. https://doi.org/10.1038/s41467-019-14136-8.

(5) Crossland, P. M.; Lien, C.-Y.; de Jong, L. O.; Spellberg, J. L.; Czaikowski, M. E.; Wang, L.; Filatov, A. S.; King, S. B.; Anderson, J. S. Processable Coordination Polymer Inks for Highly Conductive and Robust Coatings. *J. Am. Chem. Soc.* **2024**, *146* (49), 33608–33615. https://doi.org/10.1021/jacs.4c11178.

(6) Wijeyasinghe, N.; Regoutz, A.; Eisner, F.; Du, T.; Tsetseris, L.; Lin, Y. H.; Faber, H.; Pattanasattayavong, P.; Li, J.; Yan, F.; McLachlan, M. A.; Payne, D. J.; Heeney, M.; Anthopoulos, T. D. Copper(I) Thiocyanate (CuSCN) Hole-Transport Layers Processed from Aqueous Precursor Solutions and Their Application in Thin-Film Transistors and Highly Efficient Organic and Organometal Halide Perovskite Solar Cells. *Adv. Funct. Mater.* **2017**, *27* (35), 1701818. https://doi.org/10.1002/adfm.201701818.

(7) Pattanasattayavong, P.; Yaacobi-Gross, N.; Zhao, K.; Ndjawa, G. O. N.; Li, J.; Yan, F.; O'Regan, B. C.; Amassian, A.; Anthopoulos, T. D. Hole-Transporting Transistors and Circuits Based on the Transparent Inorganic Semiconductor Copper(I) Thiocyanate (CuSCN) Processed from Solution at Room Temperature. *Adv. Mater.* **2013**, *25* (10), 1504–1509. https://doi.org/10.1002/adma.201202758.

(8) Arora, N.; Dar, M. I.; Hinderhofer, A.; Pellet, N.; Schreiber, F.; Zakeeruddin, S. M.; Grätzel, M. Perovskite Solar Cells with CuSCN Hole Extraction Layers Yield Stabilized Efficiencies Greater than 20%. *Science* **2017**, *358* (6364), 768–771. https://doi.org/10.1126/science.aam5655.

(9) Chen, Y.; Zheng, Y.; Wang, J.; Zhao, X.; Liu, G.; Lin, Y.; Yang, Y.; Wang, L.; Tang, Z.; Wang, Y.; Fang, Y.; Zhang, W.; Zhu, X. Ultranarrow-Bandgap Small-Molecule Acceptor Enables Sensitive SWIR Detection and Dynamic Upconversion Imaging. *Sci. Adv.* **2024**, *10* (23), eadm9631. https://doi.org/10.1126/sciadv.adm9631.

(10) Pattanasattayavong, P.; Mottram, A. D.; Yan, F.; Anthopoulos, T. D. Study of the Hole Transport Processes in Solution-Processed Layers of the Wide Bandgap Semiconductor Copper(I) Thiocyanate (CuSCN). *Adv. Funct. Mater.* **2015**, *25* (43), 6802–6813. https://doi.org/10.1002/adfm.201502953.

(11) Pattanasattayavong, P.; Promarak, V.; Anthopoulos, T. D. Electronic Properties of Copper(I) Thiocyanate (CuSCN). *Adv. Electron. Mater.* **2017**, *3* (3), 1600378. https://doi.org/10.1002/aelm.201600378.

(12) Faber, H.; Das, S.; Lin, Y.-H.; Pliatsikas, N.; Zhao, K.; Kehagias, T.; Dimitrakopulos, G.; Amassian, A.; Patsalas, P. A.; Anthopoulos, T. D. Heterojunction Oxide Thin-Film Transistors with Unprecedented Electron Mobility Grown from Solution. *Sci. Adv.* **2017**, *3* (3), e1602640. https://doi.org/10.1126/sciadv.1602640.

(13) Park, J. W.; Kang, B. H.; Kim, H. J. A Review of Low-Temperature Solution-Processed Metal Oxide Thin-Film Transistors for Flexible Electronics. *Adv. Funct. Mater.* **2020**, *30* (20), 1904632. https://doi.org/10.1002/adfm.201904632.

(14) Charnas, A.; Zhang, Z.; Lin, Z.; Zheng, D.; Zhang, J.; Si, M.; Ye, P. D. Review-Extremely Thin Amorphous Indium Oxide Transistors. *Adv. Mater.* **2024**, *36* (9), 2304044. https://doi.org/10.1002/adma.202304044.

(15) Wijeyasinghe, N.; Eisner, F.; Tsetseris, L.; Lin, Y. H.; Seitkhan, A.; Li, J.; Yan, F.; Solomeshch, O.; Tessler, N.; Patsalas, P.; Anthopoulos, T. D. p-Doping of Copper(I) Thiocyanate (CuSCN) Hole-Transport Layers for High-Performance Transistors and Organic Solar Cells. *Adv. Funct. Mater.* **2018**, *28* (31), 1802055. https://doi.org/10.1002/adfm.201802055.

(16) Jaffe, J. E.; Kaspar, T. C.; Droubay, T. C.; Varga, T.; Bowden, M. E.; Exarhos, G. J. Electronic and Defect Structures of CuSCN. *J. Phys. Chem. C* **2010**, *114* (19), 9111–

9117. https://doi.org/10.1021/jp101586q.

(17) Tsetseris, L. Copper Thiocyanate: Polytypes, Defects, Impurities, and Surfaces. *J. Phys. Condens. Matter* **2016**, *28* (29), 295801. https://doi.org/10.1088/0953-8984/28/29/295801.

(18) Worakajit, P.; Kidkhunthod, P.; Thanasarnsurapong, T.; Waiprasoet, S.; Nakajima, H.; Sudyoadsuk, T.; Promarak, V.; Boonchun, A.; Pattanasattayavong, P. Origin of Hole-Trapping States in Solution-Processed Copper(I) Thiocyanate and Defect-Healing by I_2 Doping. *Adv. Funct. Mater.* **2023**, *33* (25), 2209504. https://doi.org/10.1002/adfm.202209504.

(19) Liang, J. W.; Firdaus, Y.; Azmi, R.; Faber, H.; Kaltsas, D.; Kang, C. H.; Nugraha, M. I.; Yengel, E.; Ng, T. K.; De Wolf, S.; Tsetseris, L.; Ooi, B. S.; Anthopoulos, T. D. Cl_2-Doped CuSCN Hole Transport Layer for Organic and Perovskite Solar Cells with Improved Stability. *ACS Energy Lett.* **2022**, *7* (9), 3139–3148. https://doi.org/10.1021/acsenergylett.2c01545.

(20) Waiprasoet, S.; Kidkhunthod, P.; Nakajima, H.; Ittisanronnachai, S.; Prayongkul, P.; Chattakoonpaisarn, C.; Songkerdthong, J.; Sukpoonprom, P.; Sudyoadsuk, T.; Promarak, V.; Pattanasattayavong, P. Doping of Copper(I) Thiocyanate (CuSCN) with Metal Chlorides for p-Channel Thin-Film Transistors. *ACS Appl. Electron. Mater.* **2024**, *6* (9), 6837–6848. https://doi.org/10.1021/acsaelm.4c01223.

(21) Lin, P.; Loganathan, A.; Raifuku, I.; Li, M.; Chiu, Y.; Chang, S.; Fakharuddin, A.; Lin, C.; Guo, T.; Schmidt-Mende, L.; Chen, P. Pseudo-Halide Perovskite Solar Cells. *Adv. Energy Mater.* **2021**, *11* (28), 2100818. https://doi.org/10.1002/aenm.202100818.

(22) Li, Z.; Wang, L.; Liu, R.; Fan, Y.; Meng, H.; Shao, Z.; Cui, G.; Pang, S. Spontaneous

Interface Ion Exchange: Passivating Surface Defects of Perovskite Solar Cells with Enhanced Photovoltage. *Adv. Energy Mater.* **2019**, *9* (38), 1902142. https://doi.org/10.1002/aenm.201902142.

(23) Liu, A.; Zhu, H.; Park, W. T.; Kang, S. J.; Xu, Y.; Kim, M. G.; Noh, Y. Y. Room-Temperature Solution-Synthesized p-Type Copper(I) Iodide Semiconductors for Transparent Thin-Film Transistors and Complementary Electronics. *Adv. Mater.* **2018**, *30* (34), 1802379. https://doi.org/10.1002/adma.201802379.

(24) Kim, C. H.; Bonnassieux, Y.; Horowitz, G. Fundamental Benefits of the Staggered Geometry for Organic Field-Effect Transistors. *IEEE Electron Device Lett.* **2011**, *32* (9), 1302–1304. https://doi.org/10.1109/LED.2011.2160249.

(25) Waiprasoet, S.; Ittisanronnachai, S.; Worakajit, P.; Sudyoadsuk, T.; Promarak, V.; Pattanasattayavong, P. Engineering High- k Oxide/CuSCN Interface for p-Channel Thin-Film Transistors. *ACS Appl. Electron. Mater.* **2024**, *6* (5), 3510–3521. https://doi.org/10.1021/acsaelm.4c00289.

(26) Worakajit, P.; Hamada, F.; Sahu, D.; Kidkhunthod, P.; Sudyoadsuk, T.; Promarak, V.; Harding, D. J.; Packwood, D. M.; Saeki, A.; Pattanasattayavong, P. Elucidating the Coordination of Diethyl Sulfide Molecules in Copper(I) Thiocyanate (CuSCN) Thin Films and Improving Hole Transport by Antisolvent Treatment. *Adv. Funct. Mater.* **2020**, *30* (36), 2002355. https://doi.org/10.1002/adfm.202002355.

(27) Liu, A.; Zhu, H.; Noh, Y. Y. Molecule Charge Transfer Doping for p-Channel Solution-Processed Copper Oxide Transistors. *Adv. Funct. Mater.* **2020**, *30* (24), 2002625. https://doi.org/10.1002/adfm.202002625.

(28) Cho, H.; Sritharan, M.; Ju, Y.; Pujar, P.; Dutta, R.; Jang, W. S.; Kim, Y. M.; Hong, S.; Yoon, Y.; Kim, S. Se-Vacancy Healing with Substitutional Oxygen in WSe_2 for High-

Mobility p-Type Field-Effect Transistors. *ACS Nano* **2023**, *17* (12), 11279–11289. https://doi.org/10.1021/acsnano.2c11567.

(29) Kalb, W. L.; Meier, F.; Mattenberger, K.; Batlogg, B. Defect Healing at Room Temperature in Pentacene Thin Films and Improved Transistor Performance. *Phys. Rev. B* **2007**, *76* (18), 184112. https://doi.org/10.1103/PhysRevB.76.184112.

(30) Zhu, J.; Hou, B.; Chen, L.; Zhu, Q.; Yang, L.; Zhou, X.; Zhang, P.; Ma, X.; Hao, Y. Threshold Voltage Shift and Interface/Border Trapping Mechanism in Al_2O_3/AlGaN/GaN MOS-HEMTs. In *IEEE International Reliability Physics Symposium Proceedings*; IEEE, 2018; Vol. 2018-March, p PWB.11-PWB.14. https://doi.org/10.1109/IRPS.2018.8353704.

(31) Paterson, A. F.; Li, R.; Markina, A.; Tsetseris, L.; Macphee, S.; Faber, H.; Emwas, A. H.; Panidi, J.; Bristow, H.; Wadsworth, A.; Baran, D.; Andrienko, D.; Heeney, M.; McCulloch, I.; Anthopoulos, T. D. n-Doping Improves Charge Transport and Morphology in the Organic Non-Fullerene Acceptor O-IDTBR. *J. Mater. Chem. C* **2021**, *9* (13), 4486–4495. https://doi.org/10.1039/d0tc05861k.

(32) Meng, Y.; Liu, G.; Liu, A.; Song, H.; Hou, Y.; Shin, B.; Shan, F. Low-Temperature Fabrication of High Performance Indium Oxide Thin Film Transistors. *RSC Adv.* **2015**, *5* (47), 37807–37813. https://doi.org/10.1039/c5ra04145g.

(33) Lee, S.; Ghaffarzadeh, K.; Nathan, A.; Robertson, J.; Jeon, S.; Kim, C.; Song, I. H.; Chung, U. I. Trap-Limited and Percolation Conduction Mechanisms in Amorphous Oxide Semiconductor Thin Film Transistors. *Appl. Phys. Lett.* **2011**, *98* (20), 203508. https://doi.org/10.1063/1.3589371.

(34) Caroli, C.; Cyrot, M.; De Gennes, P. G. ELECTRONIC TRANSPORT IN AMORPHOUS SILICON FILMS. *Phys. Rev. Lett.* **1970**, *25* (8), 509–511.

(35) Bhoolokam, A.; Nag, M.; Steudel, S.; Genoe, J.; Gelinck, G.; Kadashchuk, A.; Groeseneken, G.; Heremans, P. Conduction Mechanism in Amorphous InGaZnO Thin Film Transistors. *Jpn. J. Appl. Phys.* **2016**, *55* (1), 014301. https://doi.org/10.7567/JJAP.55.014301.

(36) Waldrip, M.; Jurchescu, O. D.; Gundlach, D. J.; Bittle, E. G. Contact Resistance in Organic Field-Effect Transistors: Conquering the Barrier. *Adv. Funct. Mater.* **2020**, *30* (20), 1904576. https://doi.org/10.1002/adfm.201904576.

(37) Liu, C.; Xu, Y.; Li, Y.; Scheideler, W.; Minari, T. Critical Impact of Gate Dielectric Interfaces on the Contact Resistance of High-Performance Organic Field-Effect Transistors. *J. Phys. Chem. C* **2013**, *117* (23), 12337–12345. https://doi.org/10.1021/jp4023844.

(38) Paterson, A. F.; Mottram, A. D.; Faber, H.; Niazi, M. R.; Fei, Z.; Heeney, M.; Anthopoulos, T. D. Impact of the Gate Dielectric on Contact Resistance in High-Mobility Organic Transistors. *Adv. Electron. Mater.* **2019**, *5* (5), 1800723. https://doi.org/10.1002/aelm.201800723.

(39) Shannon, R. D. Revised Effective Ionic Radii and Systematic Studies of Interatomic Distances in Halides and Chalcogenides. *Acta Crystallogr. Sect. A* **1976**, *32* (5), 751–767. https://doi.org/10.1107/S0567739476001551.

(40) Iwadate, Y.; Kawamura, K.; Igarashi, K.; Mochinaga, J. Effective Ionic Radii of NO_2- and SCN- Estimated in Terms of the Böttcher Equation and the Lorentz-Lorenz Equation. *J. Phys. Chem.* **1982**, *86* (26), 5205–5208. https://doi.org/10.1021/j100223a028.

(41) Worakajit, P.; Sudyoadsuk, T.; Promarak, V.; Saeki, A.; Pattanasattayavong, P. Antisolvent Treatment of Copper(I) Thiocyanate (CuSCN) Hole Transport Layer for

Efficiency Improvements in Organic Solar Cells and Light-Emitting Diodes. *J. Mater. Chem. C* **2021**, *9* (32), 10435–10442. https://doi.org/10.1039/d1tc02897a.

(42) Liu, A.; Nie, S.; Liu, G.; Zhu, H.; Zhu, C.; Shin, B.; Fortunato, E.; Martins, R.; Shan, F. In Situ One-Step Synthesis of p-Type Copper Oxide for Low-Temperature, Solution-Processed Thin-Film Transistors. *J. Mater. Chem. C* **2017**, *5* (10), 2524–2530. https://doi.org/10.1039/c7tc00574a.

(43) Smith, D. L.; Saunders, V. I. The Structure and Polytypism of the β Modification of Copper(I) Thiocyanate. *Acta Crystallogr. Sect. B Struct. Crystallogr. Cryst. Chem.* **1981**, *37* (10), 1807–1812. https://doi.org/10.1107/s0567740881007309.

(44) Packwood, D. M.; Pattanasattayavong, P. Disorder-Robust Bands from Anisotropic Orbitals in a Coordination Polymer Semiconductor. *J. Phys. Condens. Matter* **2020**, *32* (27), 275701. https://doi.org/10.1088/1361-648X/ab7d65.

(45) Hautier, G.; Miglio, A.; Ceder, G.; Rignanese, G.-M.; Gonze, X. Identification and Design Principles of Low Hole Effective Mass p-Type Transparent Conducting Oxides. *Nat. Commun.* **2013**, *4* (1), 2292. https://doi.org/10.1038/ncomms3292.

(46) Mansfield, R. Impurity Scattering in Semiconductors. *Proc. Phys. Soc. Sect. B* **1956**, *69* (1), 76–82. https://doi.org/10.1088/0370-1301/69/1/310.

(47) Wang, B.; Nam, S.; Limbu, S.; Kim, J. S.; Riede, M.; Bradley, D. D. C. Properties and Applications of Copper(I) Thiocyanate Hole-Transport Interlayers Processed from Different Solvents. *Adv. Electron. Mater.* **2022**, *8* (7), 2101253. https://doi.org/10.1002/aelm.202101253.

(48) Vasquez, R. P. CuCl by XPS. *Surf. Sci. Spectra* **1993**, *2* (2), 138–143. https://doi.org/10.1116/1.1247732.

(49) Vasquez, R. P. CuBr by XPS. *Surf. Sci. Spectra* **1993**, *2* (2), 144–148. https://doi.org/10.1116/1.1247733.

(50) Vasquez, R. P. CuI by XPS. *Surf. Sci. Spectra* **1993**, *2* (2), 149–154. https://doi.org/10.1116/1.1247734.

(51) Padam, G. K.; Malhotra, G. L.; Gupta, S. K. Study of Intrinsic Defects in Vacuum/Air Annealed $CuInSe_2$. *Sol. Energy Mater.* **1991**, *22* (4), 303–318. https://doi.org/10.1016/0165-1633(91)90037-L.

(52) Moulder, J. F.; Stickle, W. F.; Sobol, P. E. ’; Bomben, K. D.; Chastain, J. *Handbook of X-Ray Photoelectron Spectroscopy a Reference Book of Standard Spectra for Identification and Interpretation of XPS Data*; Perkin-Elmer Corporation, 1992.

(53) Stevie, F. A.; Donley, C. L. Introduction to X-Ray Photoelectron Spectroscopy. *J. Vac. Sci. Technol. A Vacuum, Surfaces, Film.* **2020**, *38* (6), 063204. https://doi.org/10.1116/6.0000412.

(54) Miller, A. C.; Simmons, G. W. Copper by XPS. *Surf. Sci. Spectra* **1993**, *2* (1), 55–60. https://doi.org/10.1116/1.1247725.

(55) Lohmann, K. B.; Motti, S. G.; Oliver, R. D. J.; Ramadan, A. J.; Sansom, H. C.; Yuan, Q.; Elmestekawy, K. A.; Patel, J. B.; Ball, J. M.; Herz, L. M.; Snaith, H. J.; Johnston, M. B. Solvent-Free Method for Defect Reduction and Improved Performance of p-i-n Vapor-Deposited Perovskite Solar Cells. *ACS Energy Lett.* **2022**, *7* (6), 1903–1911. https://doi.org/10.1021/acsenergylett.2c00865.

(56) Yu, H.; Wang, F.; Xie, F.; Li, W.; Chen, J.; Zhao, N. The Role of Chlorine in the Formation Process of “$CH_3NH_3PbI_{3-x}Cl_x$” Perovskite. *Adv. Funct. Mater.* **2014**, *24* (45), 7102–7108. https://doi.org/10.1002/adfm.201401872.

(57) Baker, M. L.; Mara, M. W.; Yan, J. J.; Hodgson, K. O.; Hedman, B.; Solomon, E. I. K- and L-Edge X-Ray Absorption Spectroscopy (XAS) and Resonant Inelastic X-Ray Scattering (RIXS) Determination of Differential Orbital Covalency (DOC) of Transition Metal Sites. *Coord. Chem. Rev.* **2017**, *345*, 182–208. https://doi.org/10.1016/j.ccr.2017.02.004.

(58) Kau, L. S.; Spira-Solomon, D. J.; Penner-Hahn, J. E.; Hodgson, K. O.; Solomon, E. I. X-Ray Absorption Edge Determination of the Oxidation State and Coordination Number of Copper. Application to the Type 3 Site in Rhus Vernicifera Laccase and Its Reaction with Oxygen. *J. Am. Chem. Soc.* **1987**, *109* (21), 6433–6442. https://doi.org/10.1021/ja00255a032.

(59) Wechwithayakhlung, C.; Wannapaiboon, S.; Na-Phattalung, S.; Narabadeesuphakorn, P.; Tanjindaprateep, S.; Waiprasoet, S.; Imyen, T.; Horike, S.; Pattanasattayavong, P. Mixed-Metal Cu-Zn Thiocyanate Coordination Polymers with Melting Behavior, Glass Transition, and Tunable Electronic Properties. *Inorg. Chem.* **2021**, *60* (21), 16149–16159. https://doi.org/10.1021/acs.inorgchem.1c01813.

(60) Azzam, S. A.; Boubnov, A.; Hoffman, A. S.; López-Ausens, T.; Chiang, N.; Canning, G.; Sautet, P.; Bare, S. R.; Simonetti, D. A. Insights into Copper Sulfide Formation from Cu and S K Edge XAS and DFT Studies. *Inorg. Chem.* **2020**, *59* (20), 15276–15288. https://doi.org/10.1021/acs.inorgchem.0c02232.

(61) Guda, A. A.; Guda, S. A.; Martini, A.; Kravtsova, A. N.; Algasov, A.; Bugaev, A.; Kubrin, S. P.; Guda, L. V.; Šot, P.; van Bokhoven, J. A.; Copéret, C.; Soldatov, A. V. Understanding X-Ray Absorption Spectra by Means of Descriptors and Machine Learning Algorithms. *npj Comput. Mater.* **2021**, *7* (1), 203. https://doi.org/10.1038/s41524-021-00664-9.

(62) Prestipino, C.; Regli, L.; Vitillo, J. G.; Bonino, F.; Damin, A.; Lamberti, C.; Zecchina, A.; Solari, P. L.; Kongshaug, K. O.; Bordiga, S. Local Structure of Framework Cu(II) in HKUST-1 Metallorganic Framework: Spectroscopic Characterization upon Activation and Interaction with Adsorbates. *Chem. Mater.* **2006**, *18* (5), 1337–1346. https://doi.org/10.1021/cm052191g.

(63) Zhao, Z.; Yang, H.; Zhu, Y.; Luo, S.; Ma, J. Interfacial N-Cu-S Coordination Mode of CuSCN/C_3N_4 with Enhanced Electrocatalytic Activity for Hydrogen Evolution. *Nanoscale* **2019**, *11* (27), 12938–12945. https://doi.org/10.1039/c9nr02860a.

(64) Ji, W.; Yue, G. Q.; Ke, F. S.; Wu, S.; Zhao, H. Bin; Chen, L. Y.; Wang, S. Y.; Jia, Y. Electronic Structures and Optical Properties of CuSCN with Cu Vacancies. *J. Korean Phys. Soc.* **2012**, *60* (8), 1253–1257. https://doi.org/10.3938/jkps.60.1253.

Data availability

The data supporting this article have been included as part of the Supplementary Information.